

Lee, H.S. J. and York, C. B. (2020) Compression and shear buckling performance of finite length plates with bending-twisting coupling. *Composite Structures*, 241, 112069.
(doi: [10.1016/j.compstruct.2020.112069](https://doi.org/10.1016/j.compstruct.2020.112069))

The material cannot be used for any other purpose without further permission of the publisher and is for private use only.

There may be differences between this version and the published version. You are advised to consult the publisher's version if you wish to cite from it.

<http://eprints.gla.ac.uk/181602/>

Deposited on 25 February 2020

Enlighten – Research publications by members of the University of
Glasgow
<http://eprints.gla.ac.uk>

COMPRESSION AND SHEAR BUCKLING PERFORMANCE OF FINITE LENGTH PLATES WITH BENDING-TWISTING COUPLING

H. S. Jason Lee¹ and Christopher B. York²

¹University of Glasgow, School of Engineering, University Avenue, Glasgow, Scotland, G12 8QQ.

²Singapore Institute of Technology, Dover Drive, Singapore 138683

Abstract

This article investigates the compression and shear buckling performance of finite length *Bending-Twisting* coupled laminated plates with simply supported edges. New contour maps are developed, representing non-dimensional buckling factors, which are superimposed on the lamination parameter design spaces for laminates with standard ply orientations. Changes in buckling mode for finite length plates complicate the contour maps, which are shown to be continuous only within discrete regions of the lamination parameter design space and are strongly influenced by plate aspect ratio. The contour maps also serve to demonstrate the degrading effect of *Bending-Twisting* coupling on compression buckling performance as well as providing new insights into shear buckling performance improvements, including optima that are non-intuitive. The adoption of two recently developed laminate databases, to which common design rules are now applied, including ply percentages and ply contiguity constraints, ensure that the conclusions drawn are based on practical rather than hypothetical designs.

Keywords

Bending-Twisting coupling; Buckling contours; Compression Buckling; Lamination Parameters; Laminate Stacking Sequences; Shear Buckling.

Nomenclature

\mathbf{A}, A_{ij}	= extensional stiffness matrix and its elements ($i,j = 1, 2, 6$)
\mathbf{B}, B_{ij}	= coupling stiffness matrix and its elements ($i,j = 1, 2, 6$)
\mathbf{D}, D_{ij}	= bending stiffness matrix and its elements ($i,j = 1, 2, 6$)
$E_{1,2}, G_{12}$	= in-plane Young's moduli and shear modulus
H	= laminate thickness (= number of plies, $n \times$ ply thickness, t)
k_x, k_{xy}	= non-dimensional buckling load factor in compression and shear
\mathbf{M}	= vector of moment resultants ($= \{M_x, M_y, M_{xy}\}^T$)
\mathbf{N}	= vector of force resultants ($= \{N_x, N_y, N_{xy}\}^T$)
m	= number of buckling half-waves ($= 1, 2, 3, \dots$), see Eq. (10)
n	= number of plies in laminate stacking sequence
n_{\pm}	= extensional stiffness parameter for angle-ply sub-sequence
n_+, n_-	= extensional stiffness parameter for positive/negative angle-ply sub-sequence
n_o, n_{\bullet}	= extensional stiffness parameter for cross-ply sub-sequences
Q_{ij}	= reduced stiffness ($i,j = 1, 2, 6$)
Q'_{ij}	= transformed reduced stiffness ($i,j = 1, 2, 6$)
t	= ply thickness
U_i	= laminate invariant ($i = 1,2,3,4,5$)
x,y,z	= principal axes

$\boldsymbol{\varepsilon}$	=	vector of in-plane strains ($= \{\varepsilon_x, \varepsilon_y, \gamma_{xy}\}^T$)
$\boldsymbol{\kappa}$	=	vector of curvatures ($= \{\kappa_x, \kappa_y, \kappa_{xy}\}^T$)
ν_{ij}	=	Poisson ratio ($i, j = 1, 2$)
θ_k	=	ply orientation for layer k
ξ_{1-2}	=	lamination parameters for extensional stiffness
ξ_{9-12}	=	lamination parameters for bending stiffness
ζ	=	bending stiffness parameter for laminate ($= n^3$)
ζ_{\pm}	=	bending stiffness parameter for angle-ply sub-sequence
ζ_+, ζ_-	=	bending stiffness parameter for positive/negative angle-ply sub-sequence
ζ_o, ζ_{\bullet}	=	bending stiffness parameter for cross-ply sub-sequences
$+, -, \pm$	=	angle plies, used in stacking sequence definition
O, \bullet	=	cross-ply, used in stacking sequence definition

1. Introduction

Degradation in the buckling performance of composite plates or panel structures occurs whenever the material exhibits *Bending-Twisting* coupling [1,2], which commonly arises in symmetric laminate designs. However, the effect of *Bending-Twisting* coupling continues to be ignored on the basis that the effects dissipate for laminates with a large number of plies. However, fuselage panels typically have between 12 and 16 plies and wing panels may have less than 17 plies in buckling critical regions, for which compression buckling strength may be overestimated (unsafe) and shear buckling strength may be overestimated or underestimated (over-designed) if the effects of *Bending-Twisting* coupling are ignored.

Earlier studies on the effect of *Bending-Twisting* coupling on finite length plates with simply supported edges adopted non-dimensional parameters [3], as indeed have the most recent studies [4], which differ from the lamination parameters used here, and by others [5-6], to aid optimum design. Furthermore, the buckling factor results presented were normalised by a bending stiffness parameter, which varies across the designs space, hence buckling performance was not directly comparable.

Laminate databases containing *Extension-Shearing* [1] and/or *Bending-Twisting* coupling [2] properties demonstrate that the design spaces contain predominantly non-symmetric stacking sequences. Heuristic design rules are now applied to these databases [7], including the adoption of symmetric stacking sequences, ply percentages and contiguity constraints to provide practical rather than hypothetical designs, from which meaningful buckling performance characteristics can be assessed.

A set of high-fidelity orthographic projections of the lamination parameter design space provide further detail of the significance of ply percentages and contiguity constraints, which

are later discussed in the context of the effect that these in-plane material constraints have on the out-of-plane design space, with specific reference to *Bending-Twisting* coupling.

Finally, new insights into compression and shear buckling performance are provided via buckling factor contour maps, which are superimposed onto the lamination parameter design spaces. Contour mapping is applied to cross-sections throughout the design space, to allow detailed interrogation of the effects of *Bending-Twisting* coupling on buckling strength. The mapping is also applied to external surfaces of the feasible domain of lamination parameters, on which some of the designs are found, since these bounding surfaces also corresponds to bounds on buckling strength. The results are applicable to finite length plates, across a range of aspect ratios, and complement a similar study on infinitely long plates with simply supported edges [8], which provide lower bound solutions to the finite length plate results. The results are useful for preliminary design, where optimised lamination parameters can be quickly matched to practical designs.

The relationship between simple supports and other boundary conditions is now well understood [9] and is covered extensively in the literature, albeit predominantly for metallic (isotropic) plates. This article therefore adopts an equivalent isotropic laminate datum to bridge the gap between metallic and composite behaviour.

There are also many published results dealing with the minimum mass design or optimisation of laminated composite plate assemblies or build up structure subject to buckling constraints. Optimisation procedures for stiffened panels generally lead to coincident buckling modes, i.e., the overall and local modes share the same buckling load [10]. An exception to this is when constraints are applied to the stiffener height, leading overall modes developing far below the local buckling load [11]. However, buckling behaviour cannot be generalized in such cases, because it is configuration dependent. Results from the current study, assuming finite length plates, and from the earlier study, assuming infinitely long plates, are applicable where plate

assemblies exhibit local buckling of the individual flat plates between stiffeners. Hence the influence of aspect ratio on the degradation in buckling strength, as a result of (poor) choice laminate design, is a primary focus of the study, since the behaviour of finite length plates is found to be very different from that of long panels.

2. Design space interrogation

The database for *Bending-Twisting* coupled designs with up to 21 plies is presented graphically in Figs 1 and 2. Figure 1(a) illustrates the lamination parameter point cloud for extensional stiffness, where each of the 112 unique points represent many individual laminate designs sharing the same proportion of standard ply orientations, i.e. 0° , 90° and $\pm 45^\circ$ plies, but with different stacking sequences. The contents of the database are also summarised in Table 1. Here the 10% rule has been applied, which corresponds to the minimum number of plies in each of the standard ply orientations. It defines a reduced region within which the lamination parameter point cloud is now constrained. The bounds of the 10% rule form a triangular plane within the feasible region of the design space given that the extensional stiffness is uncoupled. Ply contiguity further constrains the available design space, which is set to a maximum of 3 adjacent plies with the same orientation, as is now common design practice. These results reveal that the contiguity constraint closely matches the 10% rule constraint across all ply number groupings.

The lamination parameter point clouds for bending stiffness are illustrated in the orthographic projections of Fig. 2. Here, the effect of the 10% rule is seen to have limited impact, since the point cloud extends to the bounds of the feasible region.

Whilst the use of standard ply orientations was chosen primarily because they conform to common design practice, this also permits an otherwise 4-dimensional design space [6] to be represented in 3-dimensions, resulting in a design space defined by a regular tetrahedron, see Fig. 1(b).

In the original derivation of the database, all stacking sequences designs possess a single outer surface angle ply, as is common design practice, to improve damage tolerance, but this also serves to eliminate the possibility of generating cross-ply only designs. The resulting design space therefore appears to be skewed toward the positive region of the lamination parameter design space, defined by lamination parameter ξ_{11} , representing the magnitude of *Bending-Twisting* coupling, as seen in the plan view of Fig. 2. If the signs of all the angle plies are switched, such that there is now a negative outer surface angle ply, the design space will be skewed towards the negative region. Designs that represent merely a switch in the sign of the ply angles are not unique and since the stacking sequences are listed in symbolic form ($\bigcirc/+/-/\bullet$), the designer has complete freedom to choose both the sign and the value of the ply angles. For the compression buckling design charts that follow, the results are unaffected by a sign switch in the angle plies, but for the corresponding shear buckling design charts a sign switch is equivalent to reversing the shear load direction, hence both positive and negative shear buckling charts are illustrated.

2.1 Stiffness and Lamination parameter relationships

Ply angle dependent lamination parameters are now commonly adopted in design practice since they allow extensional and bending stiffness to be expressed as a set of linear design variables within convenient bounds. However, optimized lamination parameters must still be matched to a corresponding laminate configuration within the feasible region, and this is aided by graphical representations and laminate listings provided in an earlier article in this series [2].

Non-dimensional parameters from which the extensional $[A]$ and bending $[D]$ stiffness matrices can be calculated, were also developed in the earlier article, and to match the compactness of the data presented in the definitive listing of laminate stacking sequences provided for each ply number grouping, n , they were cast as:

$$A_{ij} = \{n_{\pm}Q'_{ij+} + n_oQ'_{ij0} + (n - n_{\pm} - n_o)Q'_{ij\bullet}\} \times t \quad (1)$$

$$D_{ij} = \{\zeta_{\pm}(\zeta_{+}/\zeta_{\pm})Q'_{ij+} + \zeta_{\pm}(1 - \zeta_{+}/\zeta_{\pm})Q'_{ij-} + \zeta_oQ'_{ij0} + (\zeta - \zeta_{\pm} - \zeta_o)Q'_{ij\bullet}\} \times t^3/12$$

to account for missing parameters n_{\bullet} and ζ_{\bullet} , the fact that $n_{+} = n_{-}$ in balanced laminates and the inclusion of the ratio ζ_{+}/ζ_{\pm} , indicating the degree of *Bending-Twisting* coupling. These parameters are presented together with an abridged set of stacking sequences in the electronic annex to the earlier article [2].

The non-dimensional parameters for extensional stiffness (n_o , n_{+} , n_{-} , n_{\bullet}) can be found by inspection of the laminate stacking sequence. They are simply a summation of the number of plies in each of the standard ply orientations, which can be expressed as a proportion of the total number of plies, n , and are commonly expressed as ply percentages. The non-dimensional parameters for bending stiffness require calculation, as demonstrated in the earlier article, and can also be expressed in terms of the proportion that each ply angle sub-sequence contributes to the total bending stiffness, $\zeta = n^3$.

The transformed reduced stiffness terms in Eq. (1) are given by:

$$\begin{aligned} Q'_{11} &= Q_{11}\cos^4\theta + 2(Q_{12} + 2Q_{66})\cos^2\theta\sin^2\theta + Q_{22}\sin^4\theta \\ Q'_{12} &= Q'_{21} = (Q_{11} + Q_{22} - 4Q_{66})\cos^2\theta\sin^2\theta + Q_{12}(\cos^4\theta + \sin^4\theta) \\ Q'_{16} &= Q'_{61} = \{(Q_{11} - Q_{12} - 2Q_{66})\cos^2\theta + (Q_{12} - Q_{22} + 2Q_{66})\sin^2\theta\}\cos\theta\sin\theta \\ Q'_{22} &= Q_{11}\sin^4\theta + 2(Q_{12} + 2Q_{66})\cos^2\theta\sin^2\theta + Q_{22}\cos^4\theta \\ Q'_{26} &= Q'_{62} = \{(Q_{11} - Q_{12} - 2Q_{66})\sin^2\theta + (Q_{12} - Q_{22} + 2Q_{66})\cos^2\theta\}\cos\theta\sin\theta \\ Q'_{66} &= (Q_{11} + Q_{22} - 2Q_{12} - 2Q_{66})\cos^2\theta\sin^2\theta + Q_{66}(\cos^4\theta + \sin^4\theta) \end{aligned} \quad (2)$$

and the reduced stiffness terms by:

$$\begin{aligned}
Q_{11} &= E_1/(1 - \nu_{12}\nu_{21}) \\
Q_{12} &= \nu_{12}E_2/(1 - \nu_{12}\nu_{21}) = \nu_{21}E_1/(1 - \nu_{12}\nu_{21}) \\
Q_{22} &= E_2/(1 - \nu_{12}\nu_{21}) \\
Q_{66} &= G_{12}
\end{aligned} \tag{3}$$

Lamination parameters for extensional stiffness are related to the non-dimensional parameters through the following ply orientation dependent expressions:

$$\begin{aligned}
\xi_1 &= \{n_{\pm}(n_{+}/n_{\pm})\cos(2\theta_{+}) + n_{\pm}(1 - n_{+}/n_{\pm})\cos(2\theta_{-}) + n_{\circ}\cos(2\theta_{\circ}) + n_{\bullet}\cos(2\theta_{\bullet})\}/n \\
\xi_2 &= \{n_{\pm}(n_{+}/n_{\pm})\cos(4\theta_{+}) + n_{\pm}(1 - n_{+}/n_{\pm})\cos(4\theta_{-}) + n_{\circ}\cos(4\theta_{\circ}) + n_{\bullet}\cos(4\theta_{\bullet})\}/n
\end{aligned} \tag{4}$$

and for bending stiffness through:

$$\begin{aligned}
\xi_9 &= \{\zeta_{\pm}(\zeta_{+}/\zeta_{\pm})\cos(2\theta_{+}) + \zeta_{\pm}(1 - \zeta_{+}/\zeta_{\pm})\cos(2\theta_{-}) + \zeta_{\circ}\cos(2\theta_{\circ}) + \zeta_{\bullet}\cos(2\theta_{\bullet})\}/n^3 \\
\xi_{10} &= \{\zeta_{\pm}(\zeta_{+}/\zeta_{\pm})\cos(4\theta_{+}) + \zeta_{\pm}(1 - \zeta_{+}/\zeta_{\pm})\cos(4\theta_{-}) + \zeta_{\circ}\cos(4\theta_{\circ}) + \zeta_{\bullet}\cos(4\theta_{\bullet})\}/n^3 \\
\xi_{11} &= \{\zeta_{\pm}(\zeta_{+}/\zeta_{\pm})\sin(2\theta_{+}) + \zeta_{\pm}(1 - \zeta_{+}/\zeta_{\pm})\sin(2\theta_{-}) + \zeta_{\circ}\sin(2\theta_{\circ}) + \zeta_{\bullet}\sin(2\theta_{\bullet})\}/n^3 \\
\xi_{12} &= \{\zeta_{\pm}(\zeta_{+}/\zeta_{\pm})\sin(4\theta_{+}) + \zeta_{\pm}(1 - \zeta_{+}/\zeta_{\pm})\sin(4\theta_{-}) + \zeta_{\circ}\sin(4\theta_{\circ}) + \zeta_{\bullet}\sin(4\theta_{\bullet})\}/n^3
\end{aligned} \tag{5}$$

Note that for standard ply orientations ($\circ/+/-/\bullet$) = (0/45/-45/90), lamination parameter $\xi_{12} = 0$. Note also that for balanced laminates, the extensional stiffness parameter $n_{+} = n_{-} = n_{\pm}/2$, hence Eqs (4) reduce to:

$$\begin{aligned}
\xi_1 &= \{n_{\pm}\cos(2\theta_{\pm}) + n_{\circ}\cos(2\theta_{\circ}) + n_{\bullet}\cos(2\theta_{\bullet})\}/n \\
\xi_2 &= \{n_{\pm}\cos(4\theta_{\pm}) + n_{\circ}\cos(4\theta_{\circ}) + n_{\bullet}\cos(4\theta_{\bullet})\}/n
\end{aligned} \tag{6}$$

Stacking sequence data, to which design heuristics have now been applied, are provided in the electronic annex, together with lamination parameters for standard ply angles, hence elements

of the uncoupled extensional stiffness matrix $[\mathbf{A}]$ are readily calculated using the following the lamination parameters relations [12]:

$$\begin{aligned}
A_{11} &= \{U_1 + \xi_1 U_2 + \xi_2 U_3\} \times H \\
A_{12} &= A_{21} = \{-\xi_2 U_3 + U_4\} \times H \\
A_{22} &= \{U_1 - \xi_1 U_2 + \xi_2 U_3\} \times H \\
A_{66} &= \{-\xi_2 U_3 + U_5\} \times H
\end{aligned} \tag{7}$$

and the *Bending-Twisting* coupled stiffness matrix $[\mathbf{D}]$ are readily calculated using:

$$\begin{aligned}
D_{11} &= \{U_1 + \xi_9 U_2 + \xi_{10} U_3\} \times H^3/12 \\
D_{12} &= \{U_4 - \xi_{10} U_3\} \times H^3/12 \\
D_{16} &= D_{61} = \{\xi_1 U_2/2 + \xi_{12} U_3\} \times H^3/12 \\
D_{22} &= \{U_1 - \xi_9 U_2 + \xi_{10} U_3\} \times H^3/12 \\
D_{26} &= D_{62} = \{\xi_{11} U_2/2 - \xi_{12} U_3\} \times H^3/12 \\
D_{66} &= \{-\xi_{10} U_3 + U_5\} \times H^3/12
\end{aligned} \tag{8}$$

where the laminate invariants, U_i , are given in terms of the reduced stiffnesses of Eqs (3) by:

$$\begin{aligned}
U_1 &= \{3Q_{11} + 3Q_{22} + 2Q_{12} + 4Q_{66}\}/8 \\
U_2 &= \{Q_{11} - Q_{22}\}/2 \\
U_3 &= \{Q_{11} + Q_{22} - 2Q_{12} - 4Q_{66}\}/8 \\
U_4 &= \{Q_{11} + Q_{22} + 6Q_{12} - 4Q_{66}\}/8 \\
U_5 &= \{Q_{11} + Q_{22} - 2Q_{12} + 4Q_{66}\}/8
\end{aligned} \tag{9}$$

2.2 Effect of design heuristics on the lamination parameter design space

Ply percentages are often used to account for design uncertainties relating to in-plane properties [7] and can be readily applied to the associated in-plane lamination parameter design space [14]. However, the effect of these constraints on the bending stiffness properties have not previously been investigated.

Ply percentages for standard ($0^\circ/\pm 45^\circ/90^\circ$) orientations are mapped onto the lamination parameter design space of Fig. 1(a), and are related directly to orthotropic lamination parameters, ξ_1 and ξ_2 . Typical aircraft components, such as a Spar, Skin and Stiffener, can be represented by ($0/\pm 45/90$) ply percentages (10/80/10), (44/44/12) and (60/30/10), which are in turn related to the equivalent in-plane (ξ_1, ξ_2) lamination parameters (0, -0.6), (0.32, 0.12) and (0.5, 0.4), respectively.

These typical aircraft components are plotted together with 112 unique points representing symmetrically laminated designs, with up to 21 plies, possessing *Bending-Twisting* coupling. All are contained within the 10% design rule and correspond to a ply contiguity constraint of up to 3 adjacent plies with identical orientation. Restricting the design space to a maximum of 21 plies is justified by the fact that it represents a natural limit for symmetric designs with the design heuristics applied here, i.e.: $[45_3/-45_3/0_3/90_3/0_3/-45_3/45_3]_T$, and beyond which repeating sub-laminates lead to homogenisation of the stiffness properties and a reduction in the magnitude of *Bending-Twisting* coupling. Positive ply orientation, with respect to the x-axis, is defined in Fig. 1(b).

The corresponding lamination parameter point cloud for bending stiffness is illustrated by way of the orthographic projections of Fig. 2, for which there is no discernible difference from the design space representing the entire database [2]. Each point within this 3-dimensional design space represents a coordinate from which the bending stiffness properties can be calculated

directly, and to which a stacking sequence from the laminate database can readily be matched. There are 3,404 solutions with duplicate bending stiffness properties, meaning that designs with identical bending stiffness can and do possess different extensional stiffness properties. Of course, it is well-known that designs sharing the same extensional stiffness, i.e. ply angle percentages, possess different bending stiffness properties depending on the stacking sequence. This is illustrated most dramatically in Fig. 3 for quasi-isotropic laminates, where all share a single point $(\xi_1, \xi_2) = (0, 0)$ in the lamination parameter design space for extensional stiffness. Such designs are often used for benchmarking due to the simplification of in-plane properties, but the simplification should never be assumed to extend to bending stiffness properties. For the symmetric stacking sequences considered here, quasi-isotropic properties are found exclusively within 8 and 16 ply laminates, for which there are 6 and 536 solutions. The stacking sequence listings for 16 ply laminates can be found separately in the electronic annex, together with their lamination parameter coordinates. They are grouped by matching orthotropic bending stiffness to reveal the significant differences in *Bending-Twisting* coupling magnitude, where each grouping contains between 2 and 6 stacking sequences.

Of the 93,536 designs, only 25,922 possess unique orthotropic bending stiffness properties, which corresponds to the number of points illustrated on the front elevation of the orthographic projection of Fig. 2. The entire design space is contained on 5,731 discrete parallel planes. This allows the effect of *Bending-Twisting* coupling to be studied systematically, by comparing laminates with matching orthotropic properties across. The plan view of Fig. 2 reveals that the vast majority of practical *Bending-Twisting* coupled designs are contained within the design space defined by $\xi_{11} \leq 0.5$, which informs the study on buckling performance that follows.

3. Buckling performance of finite length plates

The effect of *Bending-Twisting* coupling on the buckling performance of finite length plates with simply supported edges has previously been investigated for both compression [3] and/or shear loading [13, 16] of hypothetical designs. However, the application of design heuristics to the database of *Bending-Twisting* coupled laminates [1, 2] now permits an assessment of the buckling performance of practical design configurations.

In order to assess the vast number of designs contained in the laminate database, a closed form solution is necessary, which for compression buckling can be obtained exactly:

$$N_x = \pi^2 \left[D_{11} \left[\frac{m}{a} \right]^2 + 2(D_{12} + 2D_{66}) \frac{1}{b^2} + D_{22} \left[\frac{1}{b^4} \right] \left[\frac{a}{m} \right]^2 \right] \quad (10)$$

from knowledge of the bending stiffness, D_{ij} , plate length, a , and width, b , and the buckling half-wave parameter, m ($=1, 2, 3, \dots$), which produces the lowest critical force resultant N_x . However, Eq. (10) is only applicable to fully uncoupled laminates [15], in which $D_{16} = D_{26} = 0$, and the buckling strength for a general balanced and symmetric laminate, in which $D_{16}, D_{26} \neq 0$, can therefore be significantly overestimated (unsafe). Furthermore, there is no equivalent closed form solution for shear loaded plates. New equations must therefore be developed to assess the relative buckling performance of finite length *Bending-Twisting* coupled laminates.

The following sections therefore develop new equations applicable to both compression and shear buckling assessment of finite length rectangular plates, with simply supported boundary conditions, to complement the lower-bound solutions of the infinitely long plate [8]. The equations are then used to develop contour maps of buckling strength, which are superimposed on the lamination parameter design space to facilitate preliminary design. The contour mapping is readily applied to any cross-section throughout the design space, with constant ξ_{11} ,

to allow detailed interrogation of the effects of increasing *Bending-Twisting* coupling on buckling strength.

3.1 Contour mapping for compression buckling

For orthotropic laminates, the following buckling equation, representing a 2 dimensional, 4th order polynomial, can be solved using buckling loads obtained from the exact closed form buckling solution at 15 equally spaced points across the lamination parameter design space, as illustrated by the example cross section in Fig. 1(b), when $\xi_{11} = 0$:

$$k_x = c_1 + c_2\xi_9 + c_3\xi_{10} + c_4\xi_9^2 + c_5\xi_{10}^2 + c_6\xi_9\xi_{10} + c_7\xi_9^3 + c_8\xi_{10}^3 + c_9\xi_9\xi_{10}^2 + c_{10}\xi_9^2\xi_{10} + c_{11}\xi_9^4 + c_{12}\xi_{10}^4 + c_{13}\xi_9\xi_{10}^3 + c_{14}\xi_9^2\xi_{10}^2 + c_{15}\xi_9^3\xi_{10} \quad (11)$$

where k_x is defined by:

$$k_x = \frac{N_x b^2}{\pi^2 D_{\text{iso}}} \quad (12)$$

and D_{iso} is the bending stiffness of the equivalent isotropic laminate, defined by:

$$D_{\text{iso}} = U_I H^3 / 12 \quad (13)$$

This normalisation ensures that buckling factor results are comparable across the design space, since the relative change in buckling factor, k_x , is the same as the relative change in the critical force resultant, N_x . In this study, IM7/8552 carbon-fibre/epoxy material is used, with Young's moduli $E_1 = 161.0\text{GPa}$ and $E_2 = 11.38\text{GPa}$, shear modulus $G_{12} = 5.17\text{GPa}$ and Poisson ratio $\nu_{12} = 0.38$.

By contrast to the infinite plate results investigated previously [8], mode changes complicate the contour maps for finite length plates. Hence Eq. (11) is no longer a continuous function across the design space. The mode change boundaries must therefore first be determined, and separate equations derived for each mode region.

To help further understand the buckling mode changes across the lamination parameter design space, classical Garland curves are first presented across a range of aspect ratios (a/b) in Fig. 4. These correspond to simply supported plates subject to uniaxial compression. Here, the solid lines represent uncoupled laminate designs, whilst the broken lines represent the effect of *Bending-Twisting* coupling when $\xi_{11} = 0.5$, corresponding to the limit for practical designs.

Figure 5 illustrates contour maps with different aspect ratios, where distinct lines, disrupting the pattern of the contours, correspond to the boundary between buckling mode regions, and in turn correspond to the cusps on Fig. 4. The mode shapes for each region are illustrated above.

In Fig. 5(a), the line separates two regions representing modes with one and two longitudinal half-waves, i.e. wavelength parameters $m = 1$ and $m = 2$ in Eq. (10). This mode change is also apparent on Fig 4(a), between curves 2 and 3 at aspect ratio $a/b = 1.0$. Such boundary lines are readily determined whenever Eq. (10) is applicable, by fixing one lamination parameter coordinate and solving for the other by simply equating $N_{x,m=1}$ and $N_{x,m=2}$. The locations of the mode change at the boundaries in Fig. 4(a) correspond to $(\xi_9, \xi_{10}) = (-0.567, 0.134)$ and $(-0.691, 1)$, with buckling factor $k_x = 3.86$ and 2.95 , respectively. The same procedure can be used to confirm shape of the boundary line.

The individual curves of Fig. 4(a), with labels 1 – 5, represent discrete coordinate points along the boundary of the lamination parameter design space, as indicated by the corresponding label locations on Fig. 5(a). Figure 5(a) represents the buckling factor contour map for constant aspect ratio ($a/b = 1.0$) plates with uncoupled orthotropic bending stiffness.

Similarly, labels on the Garland curves of Figs 4(b) and (c) correspond to those on the contour maps of Figs 5(b) and (c) for aspect ratios, $a/b = 1.5$ and 2.0 , respectively. Hence, for a fixed aspect ratio, the isolines of constant buckling factor, k_x , are seen to vary with respect to the lamination parameter coordinates, or bending stiffness, as defined by Eq. (11).

The centre of the contour map represents a fully isotropic laminate, with $(\xi_9, \xi_{10}) = (0, 0)$, and corresponds to curve 8 on Figs 4(b) where $k_x = 4.00$ for aspect ratio $a/b = 1, 2, 3, \dots, \infty$. The cusps that arise from changes in buckling mode also occur at $a/b = \sqrt{2}, \sqrt{6}, \dots$ as in metallic plates [9]. However, for composite materials, the cusp locations are now strongly influenced by orthotropic bending stiffness properties; and further still by the introduction of *Bending-Twisting* coupling.

For *Bending-Twisting* coupled laminates, Eq. (10) is no longer valid and therefore a different approach must be adopted. Buckling factor (k_x) results are established at 15 sample points across the feasible region of the design space, corresponding to the grid point intersections of the triangulation illustrated on the cross-section of Fig. 1(b), from which the coefficients $c_1 - c_{15}$ in Eq. (11) can then be derived for each buckling mode.

The finite element analysis software ABAQUS [17] was used to generate buckling factor results, using the same relative grid point geometry for any cross-section throughout the lamination parameter design space with constant magnitude of *Bending-Twisting* coupling, ξ_{11} . Lamination parameters $\xi_{11} = 0$ and $\xi_{11} = 0.5$ are compared in this article since these represent the bounds for practical laminate designs. Note that $-\xi_{11}$ and $+\xi_{11}$ yield the same compression buckling factor, k_x , hence only $+\xi_{11}$ are given in Fig. 7.

The process of developing the contour maps is now briefly described with specific reference to Fig. 5(c), representing plate aspect ratio $a/b = 2.0$; chosen because it contains the highest number of mode regions. Here, individual buckling contour maps, illustrated in Fig. 6, represent the four modes of interest, but which generally require the calculation of a large number of eigenvalues at each grid point to ensure that the specific modes are found. The individual contour maps therefore represent continuous functions and, in general, all the coefficients $c_1 - c_{15}$ in Eq. (11) are non-zero. Figure 5(c) therefore comprises of the shaded

regions from each of the individual contour maps, i.e., regions containing the lowest buckling factor contours from any of the four modes. The coefficients used to generate each mode region ($m = 1, 2, 3$, and 4) in Fig 5(c), are listed in Table 2. Note that the number of significant figures in the coefficients have been reduced but are sufficient to maintain a buckling factor accurate to 2 decimal places.

Individual points on the boundary lines between mode regions are found from Eq. (11) by generating two equations using the coefficients from adjacent mode regions, m and $(m + 1)$ and then equating for a fixed lamination parameter ξ_{10} , to solve for the variable lamination parameter ξ_9 . Points on the boundary lines were also verified by individually calculating $k_{x,m}$, corresponding to the mode numbers, m , of interest, at 5 sample points along edges of the feasible region, from which two simpler polynomial equations of the following general form:

$$k_{x,m} = c_1 + c_2\xi_9 + c_3\xi_9^2 + c_4\xi_9^3 + c_5\xi_9^4 \quad (14)$$

can be generated and equated to reveal the location, ξ_9 , of coincident buckling modes, $k_{x,m} = k_{x,(m+1)}$. Equation (14) has also been used to generate the lines of each mode boundary in Fig. 5(c), using the coefficients listed in Table 3.

The accuracy of Eq. (11) was verified by seeding each mode region with 15 new sample points and recalculating the coefficients. This is an alternative approach to establishing the mode regions but requires multiple re-seeding steps to achieve convergence.

Generating buckling factor contours for finite length plates is therefore more involved than for the equivalent infinitely long plate, which require only a single continuous function:

$$k_{x,\infty} = 4.000 - 1.049\xi_{10} - 1.217\xi_9^2 + 0.340\xi_{10}\xi_9^2 - 0.360\xi_9^4 - 0.034\xi_{10}^2\xi_9^2 \quad (15)$$

which was previously printed with an error [2].

Figure 4 reveals that the mode changes occur at lower aspect ratios for *Bending-Twisting* coupled laminates in comparison to their uncoupled counterparts. The buckling curves (dotted

lines) for *Bending-Twisting* coupled laminates are also seen to descend with increasing aspect ratio and, uniquely for curve 3 with lamination parameter coordinates $(\xi_9, \xi_{10}, \xi_{11}) = (-0.5, 0, 0.5)$, ascending curves are also revealed. This is in stark contrast to the curves for uncoupled laminates (solid lines), for which the lowest point between cusps is always coincident with the asymptotic value, corresponding to the buckling load factor of the infinitely long plate.

Figure 5(a) contains a special comparison between triangular bounds for the standard ply laminates considered in this study and parabolic bounds from the literature [6] corresponding to free form angles. For non-standard or free form fibre directions, the design space changes from a 3-dimensional to a 4-dimensional relationship, which significantly complicates the mapping procedure. There is also a further reduction in buckling factor when the fibre orientations are changed from standard to non-standard angles, since ξ_{12} is now introduced. This can be demonstrated through a pseudo quasi-homogeneous quasi-isotropic *Bending-Twisting* coupled design: $[45/0/90/45/90/-45_2/0]_s$ for which all lamination parameters are zero, except $\xi_{11} = 0.4$. For finite length plates, with aspect ratios $a/b = 1.0, 1.5$ and 2.0 , the buckling factors are reduced by a further 5.2% (5.2%), 4.2% (12.1%) and 3.8% (6.0%) when the fibre directions are changed from standard $\pm 45^\circ$ plies to non-standard $\pm 30^\circ$ ($\pm 60^\circ$) plies. However, this is primarily because the lamination parameters representing orthotropic stiffnesses are now introduced, $(\xi_9, \xi_{10}) = (\pm 0.25, 0.25)$. The coupling stiffnesses remain at similar magnitudes: for $\pm 30^\circ$, $\xi_{11} = \xi_{12} = -0.34$ and; for $\pm 60^\circ$, $\xi_{11} = -\xi_{12} = -0.34$. This comparison does not therefore reveal the true influence of ξ_{12} . However, if ξ_{12} is introduced artificially, to give $(\xi_9, \xi_{10}, \xi_{11}, \xi_{12}) = (0, 0, 0.4, \pm 0.4)$, the resulting buckling factor is reduced by a further 0.6% (0.5%), -0.1% (1.1%) and -1.9% (3.5%) at aspect ratios $a/b = 1.0, 1.5$ and 2.0 , respectively.

The choice of aspect ratios presented here was strongly influenced by the plethora of results reported in the literature for isotropic plates, which represent only a single point in the centre

of the lamination parameter design space. The square and rectangular plate, with $a/b = 2$, give identical compression buckling results only when the design is representative of the (equivalent) isotropic laminate, i.e., curve 8 of Fig. 4b, or indeed for square symmetric properties, i.e., curves 6 - 10 of Fig. 4b. The results are also identical to the lower-bound solution corresponding to the infinitely long plate. For *Bending-Twisting* coupled designs, there is a very large difference in the degradation in buckling strength between these two aspect-ratios, as seen in for curve 13 of Fig. 4(c).

The rectangular plate configuration with $a/b = 1.5$ is also commonly presented in the literature. However, this aspect ratio has special significance in composite materials testing because of the requirement for compression strength after impact assessment to ASTM standard [18], with an anti-buckling requirement and for which the boundary conditions of the test are simple supports. The ASTM guidelines recommend a stacking sequence: $[45/0/-45/90]_{rs}$, but the variable number of repeats, $r = 1, 2, 3, \dots$, can be seen to possess significantly varying magnitude of *Bending-Twisting* coupling, i.e., $(\xi_9, \xi_{10}, \xi_{11}) = (0.28, -0.38, \underline{0.47})$, $(0.16, -0.19, \underline{0.21})$ and $(0.12, -0.13, \underline{0.14})$, respectively.

3.2 Contour mapping for shear buckling

Equations for shear loaded plates are obtained using the same procedure adopted for compression buckling. However, the finite element analysis software ABAQUS [17] must now be used for uncoupled as well as coupled designs to generate buckling factors at the grid point locations illustrated on Fig. 1(b).

For the uncoupled laminates, positive and negative shear give identical buckling load factor. The shear buckling factors are obtained by substituting the calculated coefficients into Eq. (10). In this case, k_{xy} is defined by:

$$k_{xy} = \frac{N_{xy} b^2}{\pi^2 D_{iso}} \quad (16)$$

The resulting contour maps are presented in Fig. 8(a) – (c), showing isolines of constant buckling load factor across the lamination parameter design space for aspect ratios $a/b = 1.0$, 1.5 and 2.0, respectively. Positive shear direction (N_{xy}) is defined together with positive fibre angle direction in Fig. 1(b). For uncoupled rectangular plates, there is no difference in the shear buckling results for positive shear or negative shear loading. However, for *Bending-Twisting* coupled rectangular plates with $\xi_{11} = 0.5$, Fig. 9 and Fig. 10 demonstrate marked differences due to shear load reversal. This can be appreciated by the fact that shear loading and *Bending-Twisting* coupling ($\xi_{11} \neq 0$) both give rise to skewed nodal lines in the buckling mode shapes [8]. Figure 9 and 10 represent the equivalent series of negative and positive shear buckling factor contour maps, respectively. In both cases, minima and maxima on the sloping boundary of the feasible design space, which often coincide with dotted lines indicating a change in buckling mode. The maximum negative shear buckling factors, $k_{xy} = 14.86$ and 10.71, are both located at $(\xi_9, \xi_{10}, \xi_{11}) = (0, -1, 0.5)$ for $a/b = 1.0$ and 1.5, whilst for $a/b = 2.0$, $k_{xy} = 9.89$ and is located at $(\xi_9, \xi_{10}, \xi_{11}) = (-0.35, -0.31, 0.5)$. By contrast, the maximum positive shear buckling factor, $k_{xy} = 7.30$, for coupled laminates with $a/b = 1.0$, is located at $(\xi_9, \xi_{10}, \xi_{11}) = (0, -1, 0.5)$, whereas for the locations at $a/b = 1.5$ and 2.0 correspond to $(\xi_9, \xi_{10}, \xi_{11}) = (0.41, -0.92, 0.5)$ and $(-0.13, -0.74, 0.5)$, with $k_{xy} = 5.30$ and 4.84, respectively.

Shear buckling results are reported in the literature [6] for optimised lamination parameters, representing hypothetical or non-standard designs. For aspect ratio $a/b = 2.0$ they have been shown to correspond to $(\xi_9, \xi_{10}) = (-0.39, -0.7)$ for orthotropic designs and $(\xi_9, \xi_{10}, \xi_{11}, \xi_{12}) = (-0.42, -0.64, -0.91, 0.77)$ for *Bending-Twisting* coupled designs, representing buckling factor results, $k_{xy} = 7.94$ and 12.51, respectively. By contrast, the maximum shear buckling factor for practical designs corresponds to $k_{xy} = 7.52$, located at $(\xi_9, \xi_{10}) = (-0.26, -0.49)$ on Fig. 8(c), for

which a stacking sequence $[45/-45_2/90/45/90_3/0]_S$ with matching lamination parameter coordinates is readily extracted from the laminate database. Similarly, stacking sequence $[45_2/90_2/-45/90/0/-45]_S$ corresponds to the maximum shear buckling factor, $k_{xy} = 9.89$, and located at $(\xi_9, \xi_{10}, \xi_{11}) = (-0.35, -0.31, 0.5)$ on Fig. 9(c). Practical designs clearly offer more modest performance benefits than optimised solutions would suggest.

Note that the optimized lamination parameters for shear buckling [6], with $a/b = 1$ and 2, were virtually the same for both simply supported and clamped conditions. The degrading influence of *Bending-Twisting* coupling on compression buckling strength was also found to be similar for both simply supported and clamped boundary conditions [2].

3.3 Surface contour mapping for compression and shear buckling

Contour mapping is applied to external surfaces of the feasible domain of lamination parameters for each of the aspect ratios $a/b = 1.0, 1.5$ and 2.0 as illustrated in Figs 11 - 13 for compression buckling and Figs 14 - 16 for (positive) shear buckling, respectively. These reveal the bounds on buckling performance for all hypothetical designs, as well as local optima away from the edges of the design space.

Figures 11 - 13 show front and side views of all four surfaces of the design space, forming a regular tetrahedron, onto which compression buckling contours are projected for aspect ratios $a/b = 1.0, 1.5$ and 2.0 are superimposed. The mode changes are denoted by dotted lines, which once again disrupt the continuity of the isolines of constant buckling load factor, as was seen in cross-sections through the design space. The effect of *Bending-Twisting* coupling, arising from $\xi_{11} \neq 0$, now introduces significant curvature into the boundaries between different mode regions, as illustrated in Fig. 11(a). The local optimum at the centre of the front and rear sloping faces represents the hypothetical limit of a pseudo quasi-homogeneous quasi-isotropic laminate, with $\xi_{11} = \pm 0.5$ and $k_x = 3.46$. The maximum buckling load factor, $k_x = 5.03$, can be

found along the bottom edge of the design space, on Fig. 11(a) and (c), but this corresponds to a fully uncoupled design. The local optimum at the centre of the front and rear sloping faces shift position with changes in aspect ratio, and corresponds to a mode change boundary in Figs 12 and 13. The variation in the optimum buckling factor for the three aspect ratios of Figs 11 - 13 can be explained by observing the behaviour of the highest garland curve across Fig. 4 at the same aspect ratios.

Figures 14 - 16 illustrate the surface contours for shear buckling with $a/b = 1.0, 1.5$ and 2.0 , respectively. Lines traced from the apex of the tetrahedron, across these surfaces, differ significantly from those of the cross section of Fig. 8, at $\xi_{11} = 0$. Similarly, surface mode changes can be compared to the cross sections of Figs 9 and 10 for negative shear (front surface) and positive shear (rear surface) at $\xi_{11} = 0.5$, respectively, and reveal the influence on mode change with increasing magnitude of *Bending-Twisting* coupling. The number and position of these mode changes also varies significantly with aspect ratio. Indeed, no mode changes are present in the surface contours for the infinitely long case [8], in which local optima were also found in locations that are non-intuitive, i.e. the optimum shear buckling factor $k_{xy,\infty} = 9.06$ at $(\xi_9, \xi_{10}, \xi_{11}) = (-0.18, -0.64, -0.82)$, which exceeds $k_{xy,\infty} = 8.84$ at $(\xi_9, \xi_{10}, \xi_{11}) = (0, -1, -1)$. For finite length plates, the hypothetical optima for $a/b = 1.0, 1.5$, and 2.0 correspond to $k_{xy} = 17.69, 12.79$ and 11.12 , respectively, and all occur at $(\xi_9, \xi_{10}, \xi_{11}) = (0, -1, -1)$.

Collectively, the cross-section and surface contour maps demonstrate the added complexity associated with laminate selection from a design space in which buckling strength is a non-continuous function. They also demonstrate that the isolines of constant buckling factor become increasingly curved with as the aspect ratio tends towards the infinitely long plate and/or magnitude ξ_{11} of *Bending-Twisting* coupling. However, for practical designs, the limits

of ξ_{11} are more realistically represented through cross sections at $\xi_{11} = 0$ and $\xi_{11} = 0.5$, which reveal optima that are non-intuitive.

These design charts can also be used in conjunction with the data in the electronic annex, which contains all 96,940 stacking sequence representing balanced and symmetric laminates with up to 21 plies and separately, the 16 ply quasi-isotropic symmetric stacking sequence listings with associated lamination parameter coordinates, grouped to aid design selection for minimising the degrading influence of *Bending-Twisting* coupling.

4. Conclusions

- Insights have been given for maximising compression and shear buckling strength for finite length plates, through the superposition of contour maps onto the lamination parameter design space for practical laminate designs with *Bending-Twisting* coupling. The non-intuitive location of local as well as global optima are revealed by inspection.
- Contour maps representing cross sections through the design space demonstrate the added complexity associated with laminate selection when buckling strength is a non-continuous function. This is due to mode changes that are dependent both on bending stiffness properties (or lamination parameter coordinate) as well as plate aspect ratio.
- The contour maps represent practical limits on buckling performance by accounting for common laminate design rules, including symmetry, standard ply angles, minimum ply percentages and maximum ply contiguity rules.
- Contour maps representing the outer surfaces of the design space demonstrate the limits on both compression and shear buckling strength as a result of the presence of *Bending-Twisting* coupling, noting that significant improvements in shear buckling strength are largely beyond what is achievable in design practice.

The raw and processed data required to reproduce these findings are available to download at
doi: 10.17632/rys232ynhf.3

References

1. C. B. York and S. F. M. Almeida, On extension-shearing bending-twisting coupled laminates, *Composite Structures*, **164**, 2017, pp. 10-22 (doi: 10.1016/j.compstruct.2016.12.041).
2. C. B. York, On bending-twisting coupled laminates, *Composite Structures*, **160**, 2017, pp. 887-900 (doi: 10.1016/j.compstruct.2016.10.063).
3. M. P. Nemeth, Importance of Anisotropy on Buckling of Compression-Loaded Symmetric Composite Plates, *AIAA Journal*, 24(11), 1986, pp. 1831-1835.
4. A. Baucke, C. Mittelstedt, Closed-form analysis of the buckling loads of composite laminates under uniaxial compressive load explicitly accounting for bending–twisting-coupling. *Composite Structures*, 128, 2015, pp. 437-454.
5. J. L. Grenestedt, Lay-up Optimisation against Buckling of Shear Panels, *Structural Optimisation*, 3(7), 1991, pp. 115-120.
6. H. Fukunaga, H. Sekine, M. Sato and A. Lino, Buckling design of symmetrically laminated plates using lamination parameters, *Computers and Structures*, 57(4), 1995, pp. 643-649.
7. J. A. Bailie, R. P. Ley, and A. Pasricha, *A summary and review of composite laminate design guidelines*, Task 22, NASA Contract NAS1-19347, 1997.
8. C. B. York and S. F. M. de Almeida, Effect of bending-twisting coupling on the compression and shear strength of infinity long plates, *Composite Structures*, 184, 2018, pp. 18-29.
9. C. B. York, Elastic buckling design curves for isotropic rectangular plates with continuity or elastic edge restraint against rotation. *Aeronautical Journal*, 104(1034), 2000, pp. 175-182.
10. M. S. Anderson and J. Stroud, General panel sizing code and its application to composite structural panels, *AIAA Journal*, 17(8), 1979, pp. 892-897.

11. C. B. York, F. W. Williams, D. Kennedy and R. Butler, A parametric study of optimum designs for benchmark stiffened wing panels. *Composites Engineering*, 3(7-8), 1993, pp. 619-632.
12. S.W. Tsai and H.T. Hahn, *Introduction to composite materials*, Technomic Publishing Co. Inc., Lancaster, 1980.
13. M. P. Nemeth, Buckling of symmetrically laminated plates with compression, shear, and in-plane bending, *AIAA Journal*, 30(12), 1992, pp. 2959-2965.
14. M. W. D. Nielsen, K. J. Johnson, A. T. Rhead and R. Butler, Laminate design for optimised in-plane performance and ease of manufacture. *Composite structures*, 177, 2018, pp. 119-128.
15. C. B. York, Characterization of non-symmetric forms of fully orthotropic laminates. *Journal of Aircraft*, 46(4), 2009, pp. 1114-1125.
16. J. Loughlan, The shear buckling behaviour of thin composite plates with particular reference to the effects of bend-twist coupling, *International Journal of Mechanical Sciences*, 43, 2001, pp. 771-792.
17. ABAQUS/Standard, Version 6.14. Dassault Systèmes Simulia Corp., 2018
18. ASTM D7137/D7137M Standard test method for compressive residual strength properties of damaged polymer matrix composite plates, 2017.

Figures

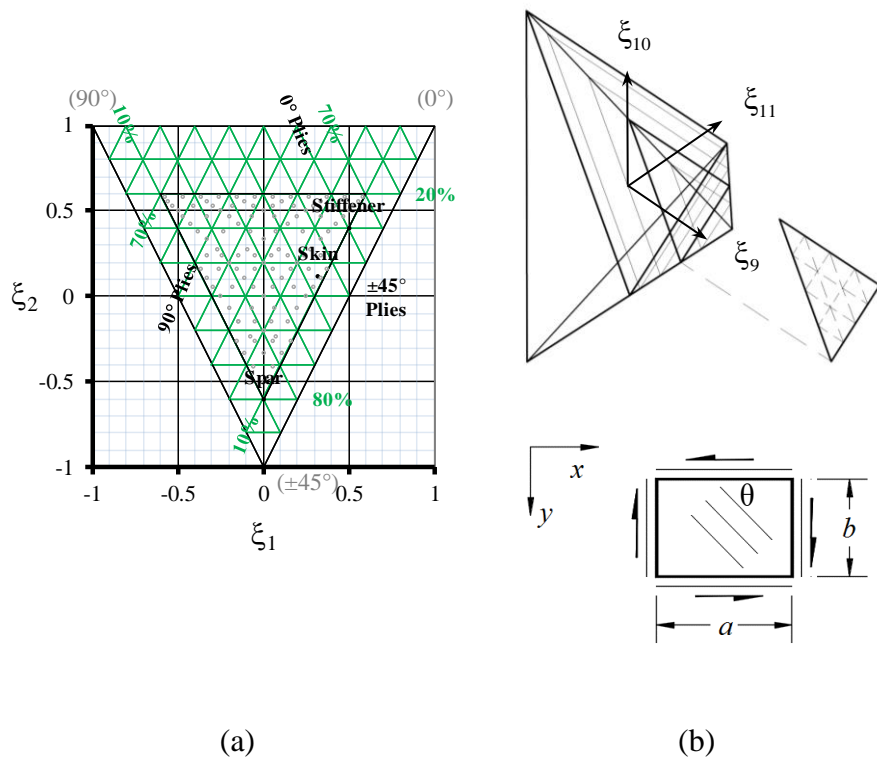


Figure 1

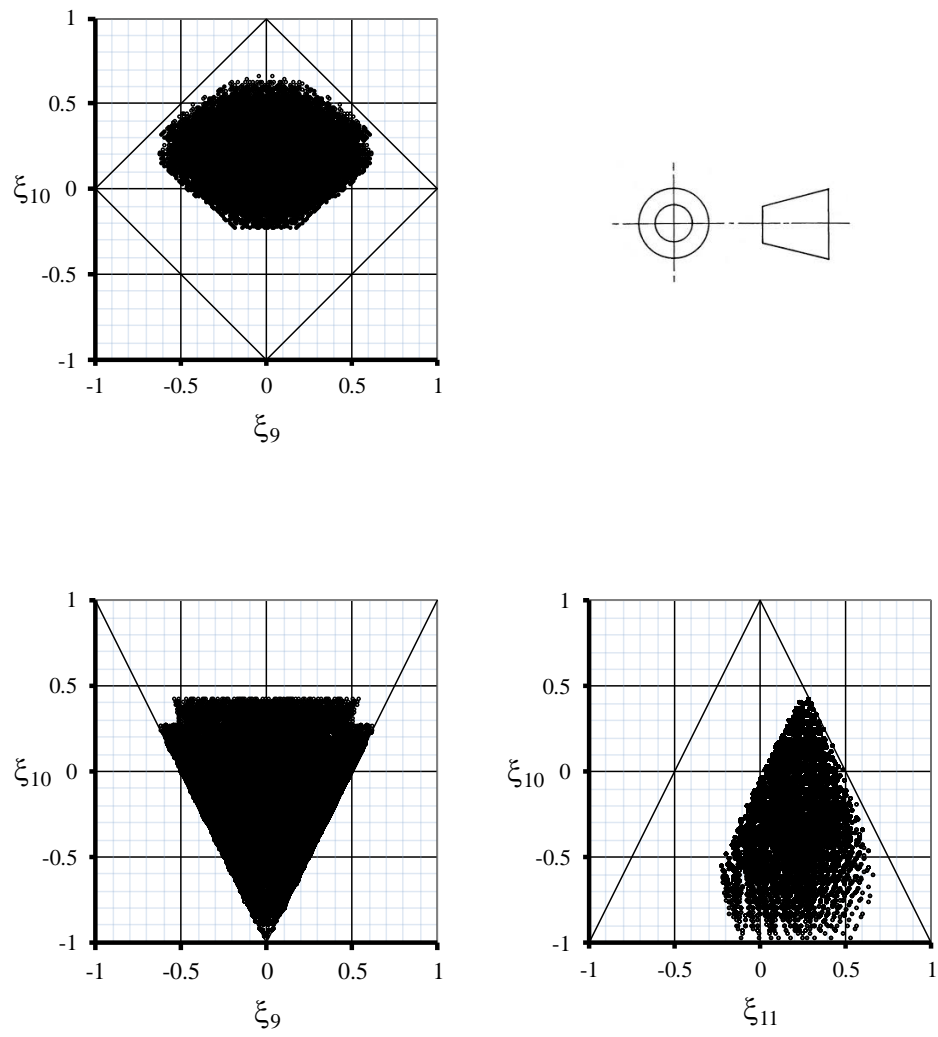


Figure 2

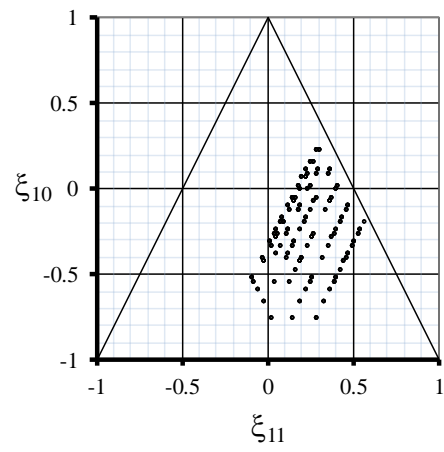
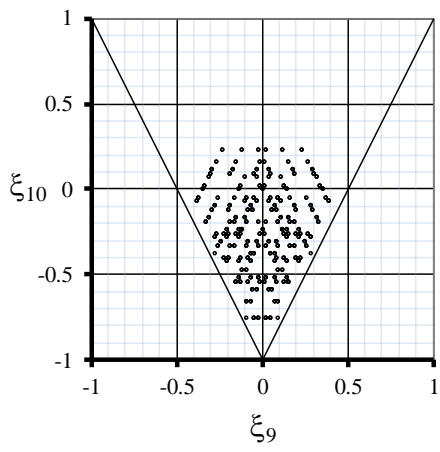
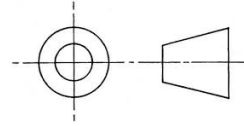
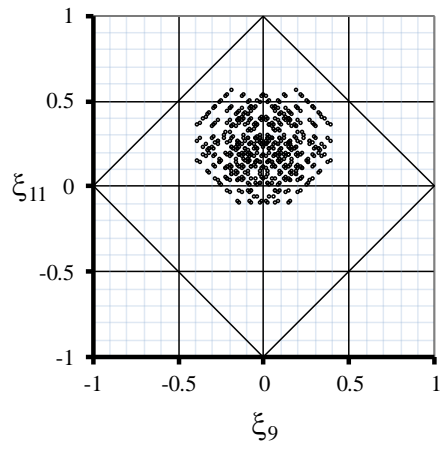
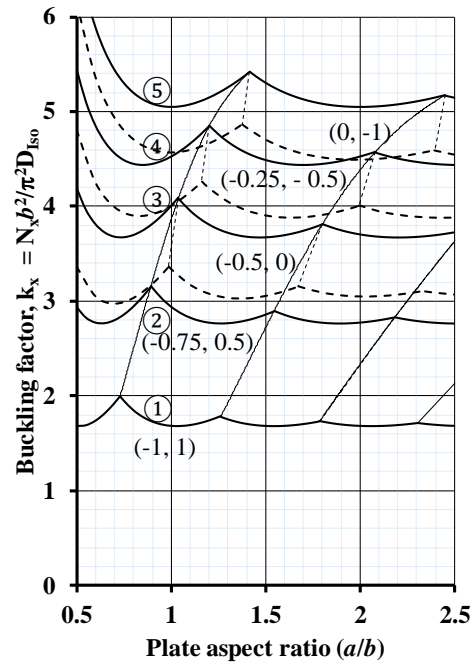
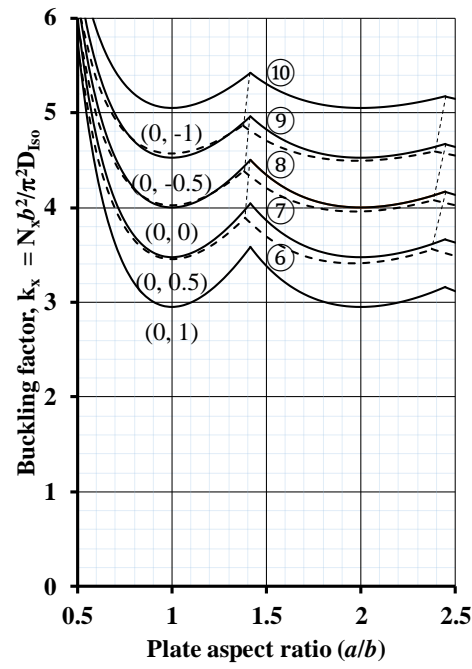


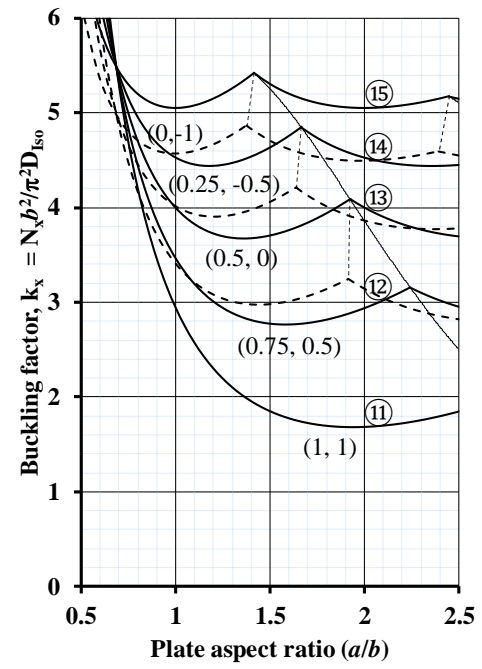
Figure 3



(a)



(b)



(c)

Figure 4

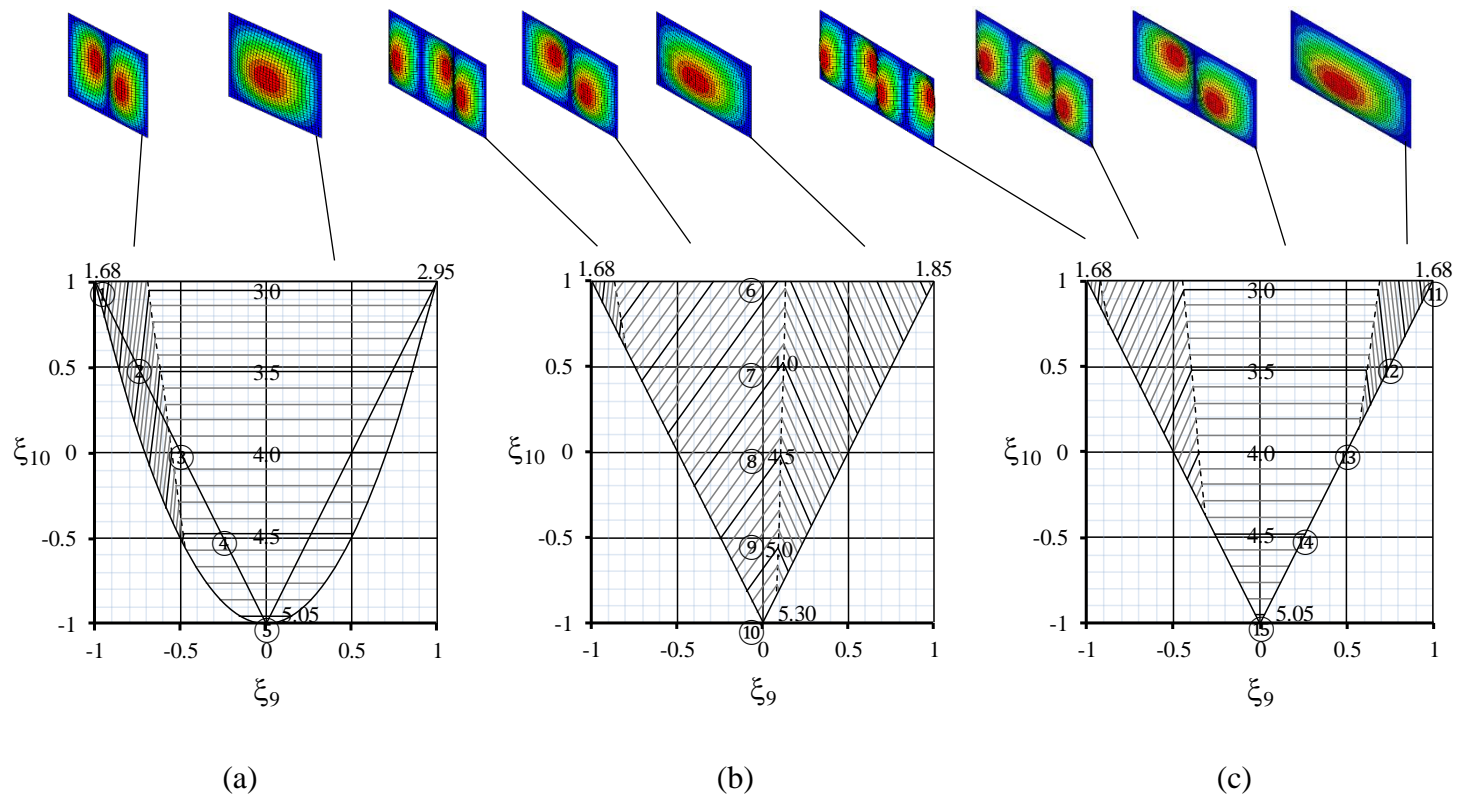
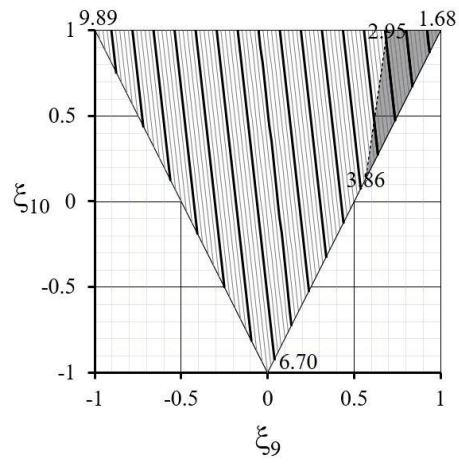
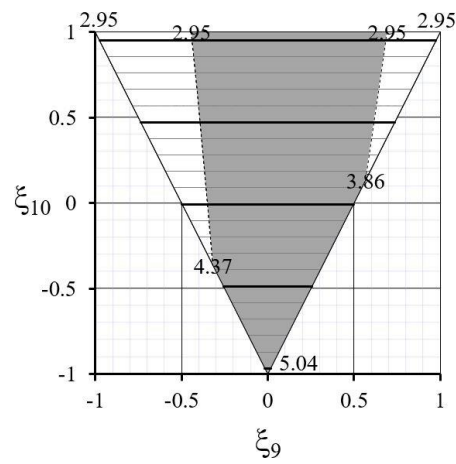


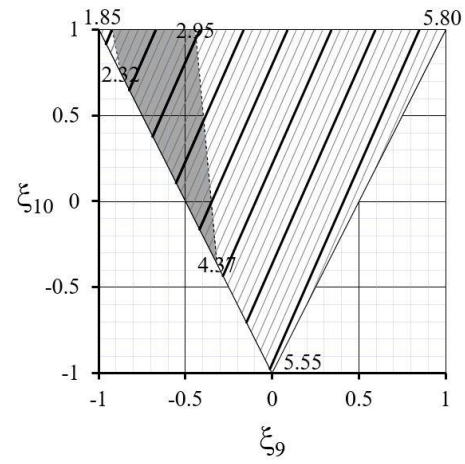
Figure 5



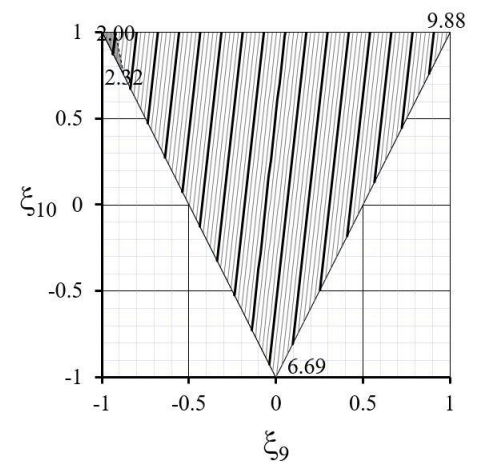
$m = 1$



$m = 2$

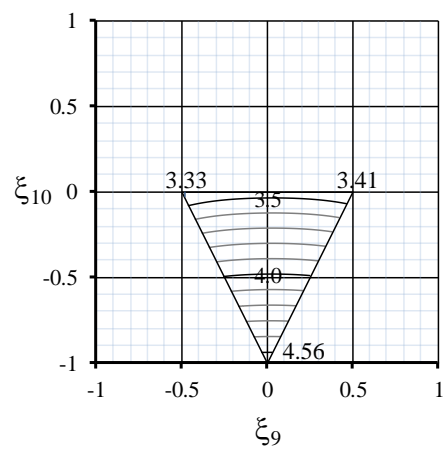


$m = 3$

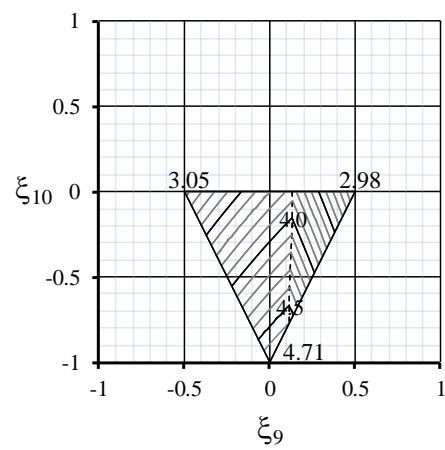


$m = 4$

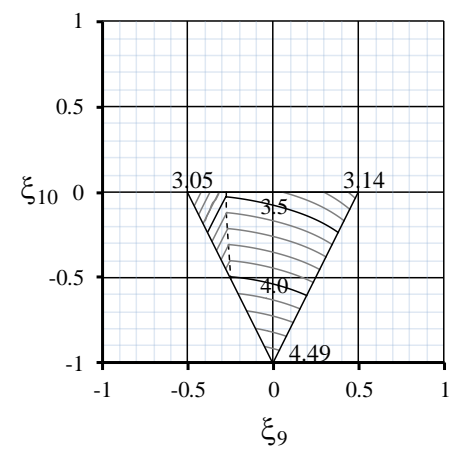
Figure 6



(a)



(b)



(c)

Figure 7

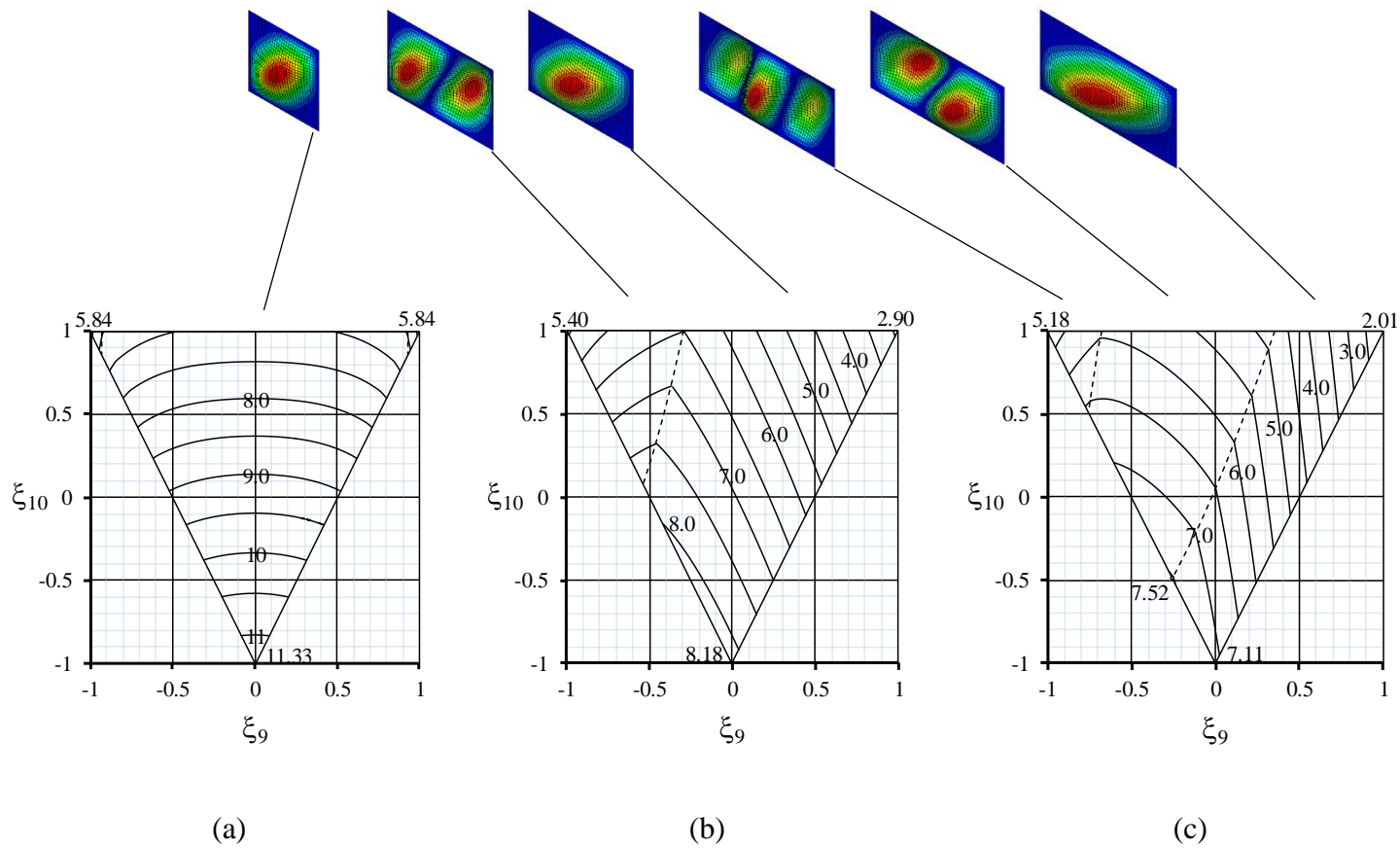
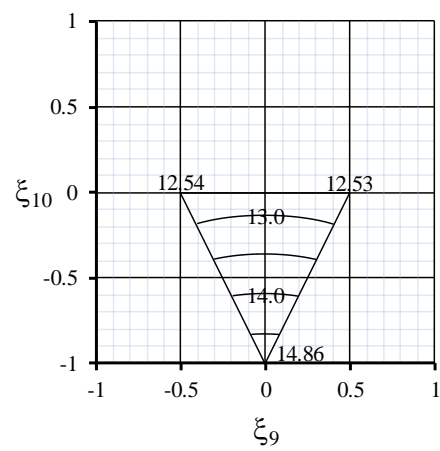
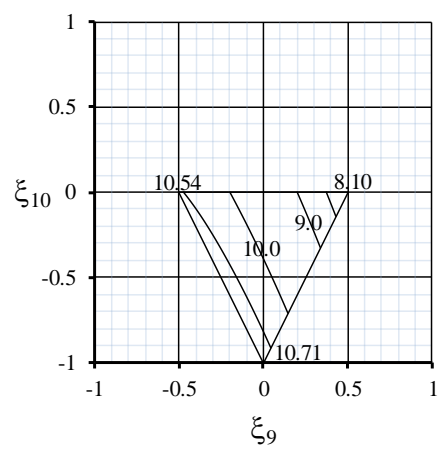


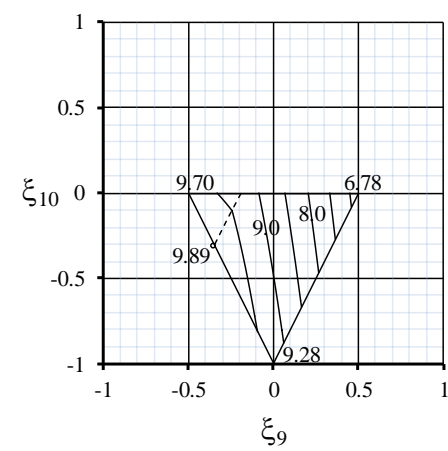
Figure 8



(a)

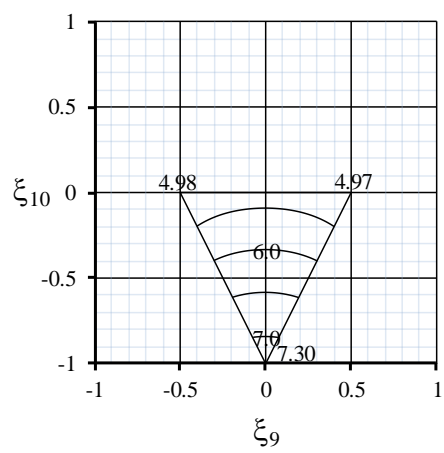


(b)

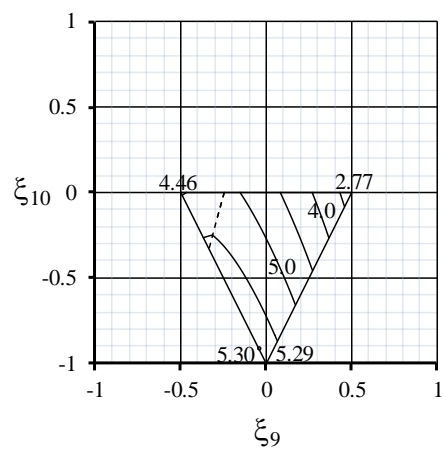


(c)

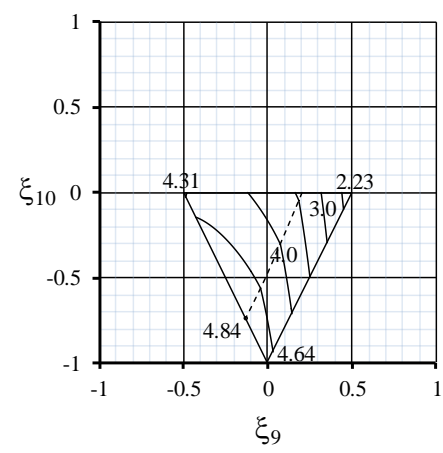
Figure 9



(a)

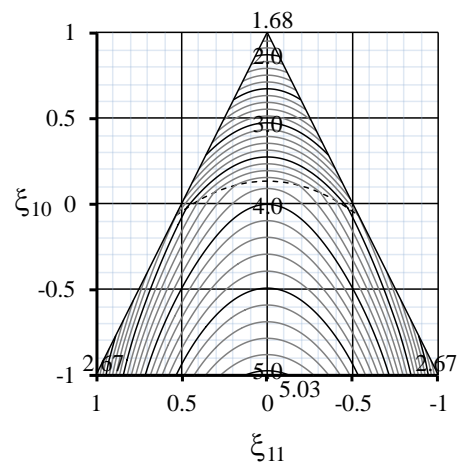


(b)

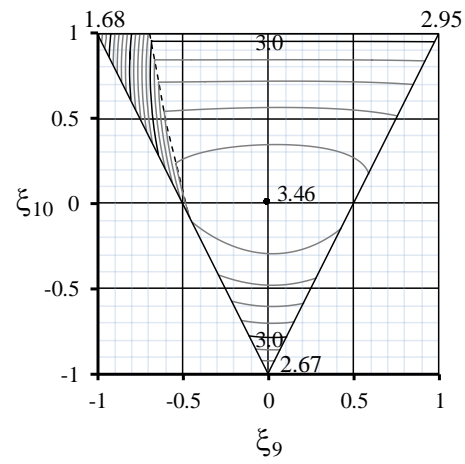


(c)

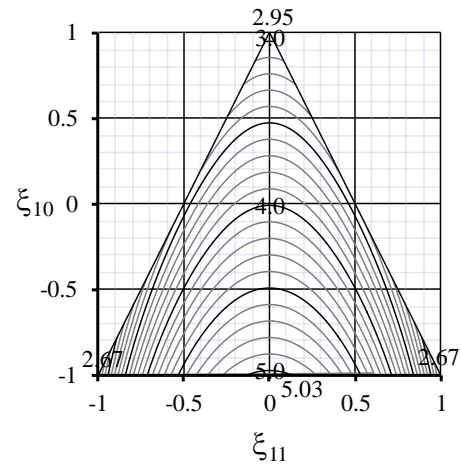
Figure 10



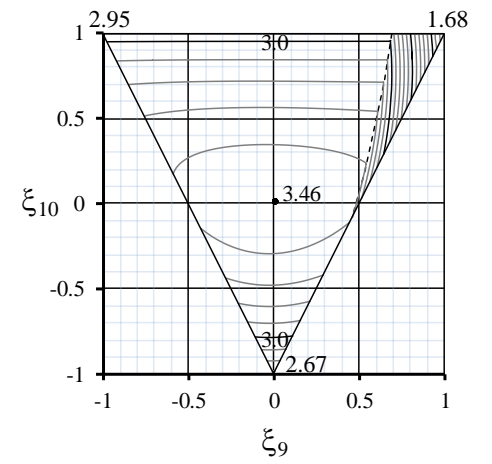
(a)



(b)

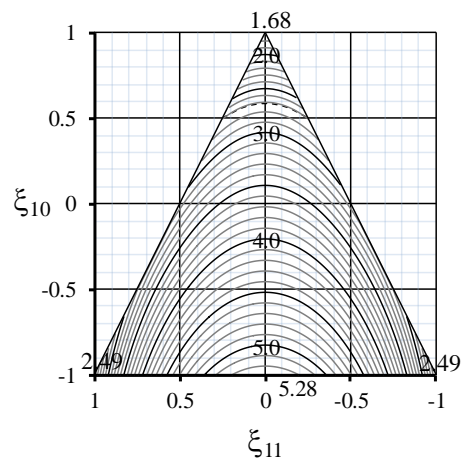


(c)

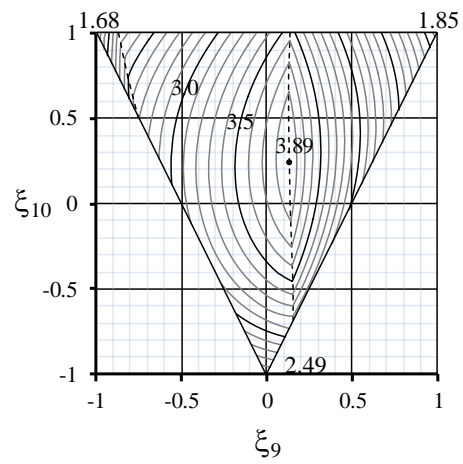


(d)

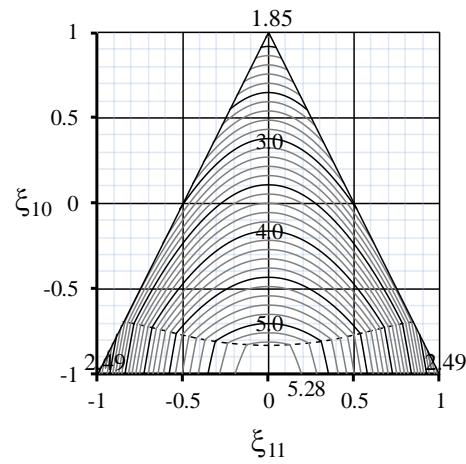
Figure 11



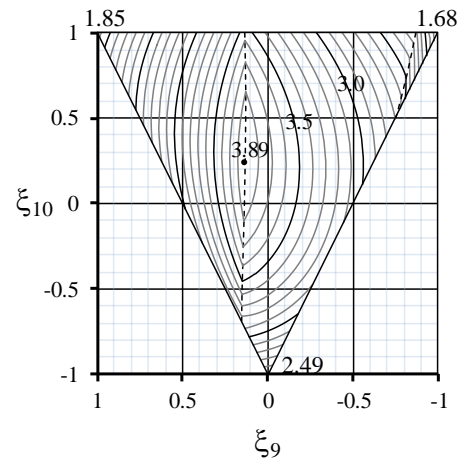
(a)



(b)

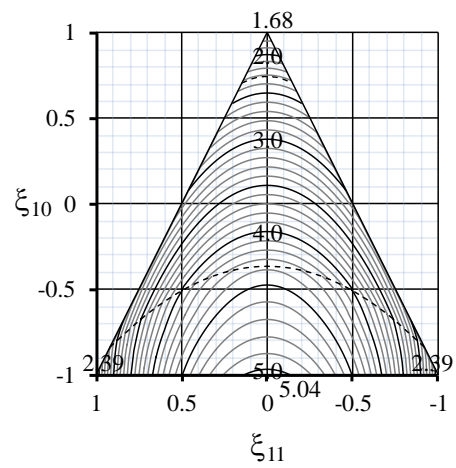


(c)

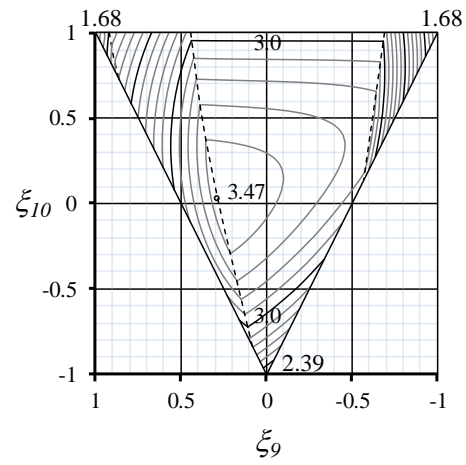


(d)

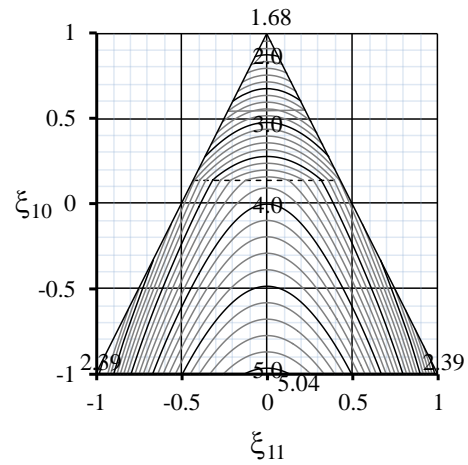
Figure 12



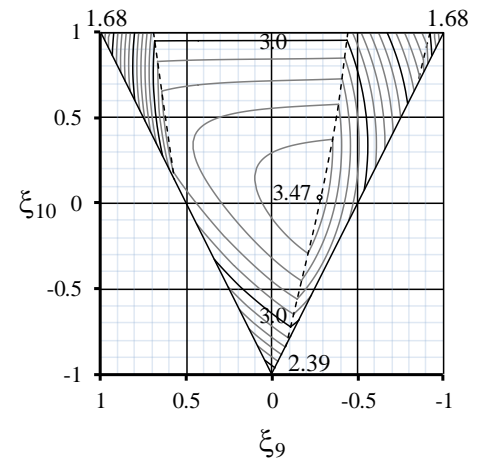
(a)



(b)

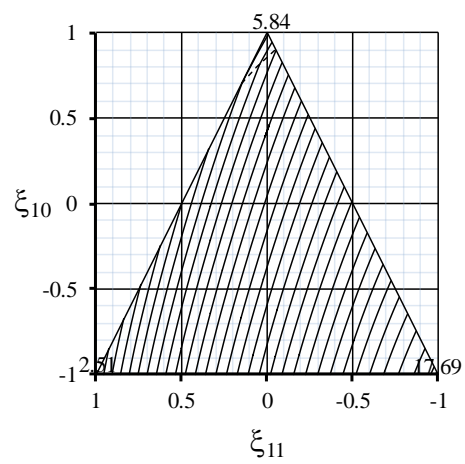


(c)

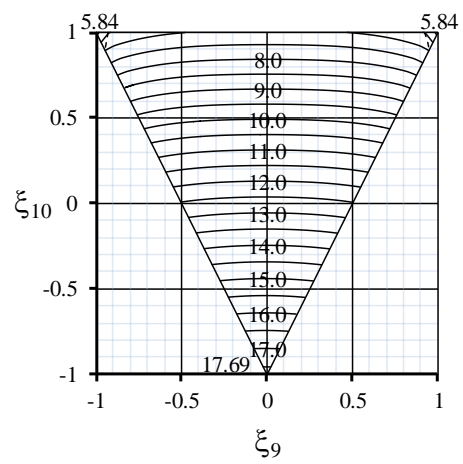


(d)

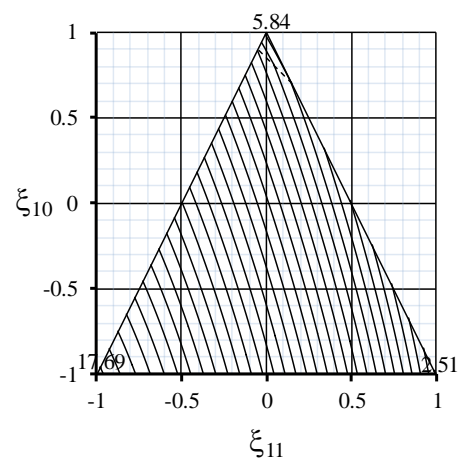
Figure 13



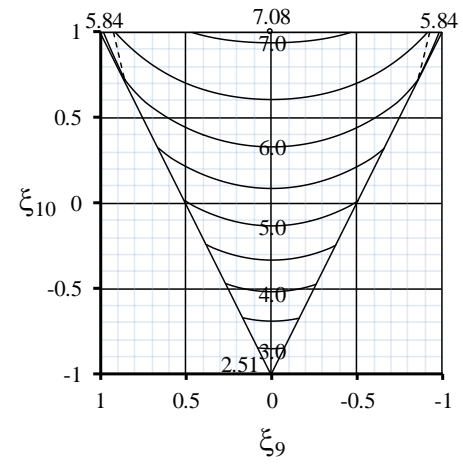
(a)



(b)

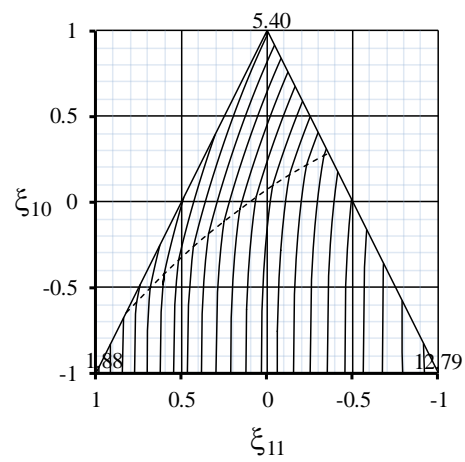


(c)

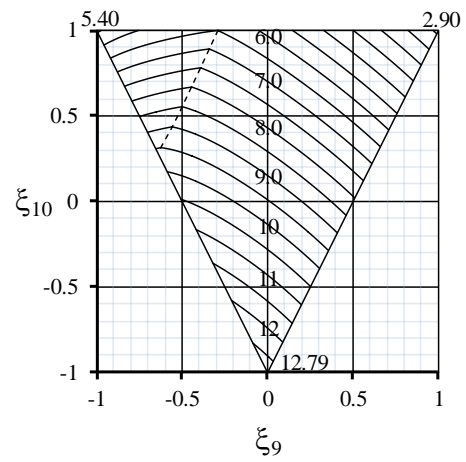


(d)

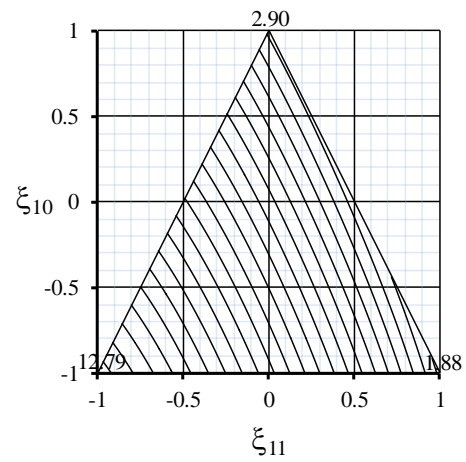
Figure 14



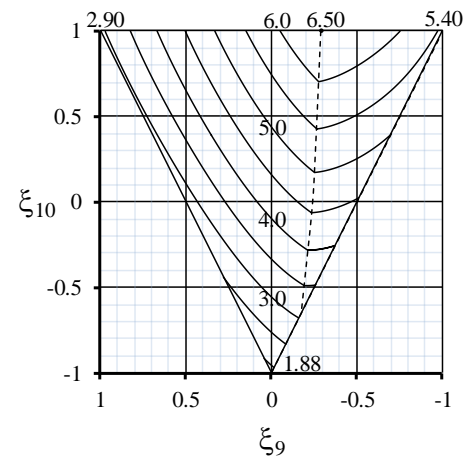
(a)



(b)

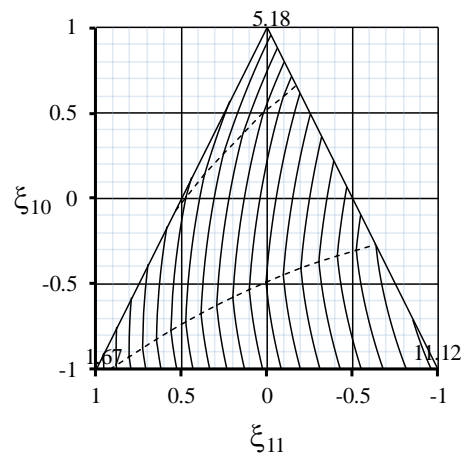


(c)

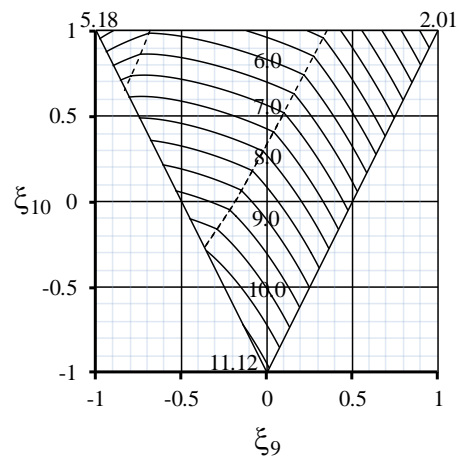


(d)

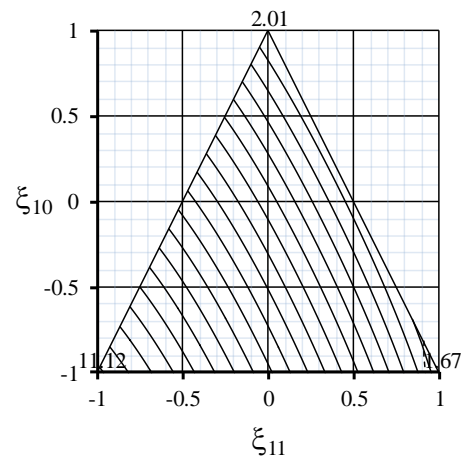
Figure 15



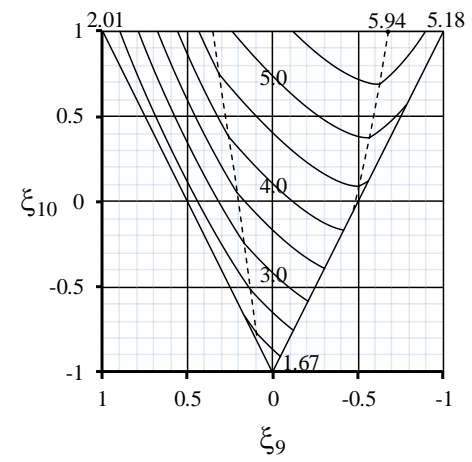
(a)



(b)



(c)



(d)

Figure 16

Figure Captions

Figure 1 - Lamination parameter design spaces for symmetric *Bending-Twisting* coupled laminates with up to 21 plies, with 10% rule and ply contiguity constraints (≤ 3) applied, corresponding to point clouds for: (a) extensional stiffness (ξ_1, ξ_2), including ply percentage mapping, and; (b) three-dimensional representation of the lamination parameter design space highlighting the locations ($\xi_{11} = 0$ and $\xi_{11} = 0.5$) through which two dimensional cross-sections have been taken and a typical 15 point grid of sample points for developing the polynomial equations. Plate axis system, positive shear load, positive fibre orientation with respect to the x-axis, and aspect ratio (a/b) are defined in the thumbnail sketch.

Figure 2 - Orthographic projections (plan, front elevation and side elevation) of point clouds for bending stiffness ($\xi_9, \xi_{10}, \xi_{11}$), corresponding to symmetric *Bending-Twisting* coupled laminates with up to 21 plies, with 10% rule and ply contiguity constraints (≤ 3) applied.

Figure 3 - Orthographic projections (plan, front elevation and side elevation) of point clouds for bending stiffness ($\xi_9, \xi_{10}, \xi_{11}$), corresponding to Quasi-Isotropic laminates.

Figure 4 - Compression buckling curves for $\xi_{11} = 0$ (solid lines) and $\xi_{11} = 0.5$ (broken lines). The corresponding lamination parameter coordinates (ξ_9, ξ_{10}) are given alongside each curve.

Figure 5 - Compression buckling contours $k_x (= N_x b^2 / \pi^2 D_{Iso})$ for $\xi_{11} = 0.0$, with: (a) $a/b = 1.0$ (including parabolic bounds after Ref. [6]); (b) $a/b = 1.5$ and; (c) $a/b = 2.0$.

Figure 6 - Compression buckling contours map construction, involving superposition of contour maps for each buckling mode, representing $m = 1, 2, 3$ and 4 in Eq. (10). Shading illustrates the extent of each mode region, corresponding to minimum k_x .

Figure 7 - Compression buckling contours, $k_x (= N_x b^2 / \pi^2 D_{Iso})$, for $\xi_{11} = 0.5$ with: (a) $a/b = 1.0$; (b) $a/b = 1.5$ and (c) $a/b = 2.0$.

Figure 8 - Positive and Negative Shear buckling factor contours, $k_{xy} (= N_{xy} b^2 / \pi^2 D_{Iso})$, for $\xi_{11} = 0.0$ with: (a) $a/b = 1.0$; (b) $a/b = 1.5$, and (c) $a/b = 2.0$.

Figure 9 - Negative Shear buckling factor contours, $k_{xy} (= N_{xy} b^2 / \pi^2 D_{Iso})$, for $\xi_{11} = 0.5$ with: (a) $a/b = 1.0$; (b) $a/b = 1.5$, and (c) $a/b = 2.0$.

Figure 10 - Positive Shear buckling factor contours, $k_{xy} (= N_{xy} b^2 / \pi^2 D_{Iso})$, for $\xi_{11} = 0.5$ with: (a) $a/b = 1.0$; (b) $a/b = 1.5$, and (c) $a/b = 2.0$.

Figure 11 - Lamination parameter design space surface contours for Compression buckling factor, $k_x (= N_x b^2 / \pi^2 D_{Iso})$, with $a/b = 1$, corresponding to: (a) Left (sloping) face; (b) Front (sloping) face; (c) Right (sloping) face and; Rear (sloping) face.

Figure 12 - Lamination parameter design space surface contours for Compression buckling factor, $k_x (= N_x b^2 / \pi^2 D_{Iso})$, with $a/b = 1.5$, corresponding to: (a) Left (sloping) face; (b) Front (sloping) face; (c) Right (sloping) face and; Rear (sloping) face.

Figure 13 - Lamination parameter design space surface contours for Compression buckling factor, $k_x (= N_x b^2 / \pi^2 D_{Iso})$, with $a/b = 2.0$, corresponding to: (a) Left (sloping) face; (b) Front (sloping) face; (c) Right (sloping) face and; Rear (sloping) face.

Figure 14 - Lamination parameter design space surface contours for Positive Shear buckling factor, $k_{xy} (= N_{xy} b^2 / \pi^2 D_{Iso})$, with $a/b = 1.0$, corresponding to: (a) Left (sloping) face; (b) Front (sloping) face; (c) Right (sloping) face and; Rear (sloping) face.

Figure 15 - Lamination parameter design space surface contours for Positive Shear buckling factor, $k_{xy} (= N_{xy}b^2/\pi^2D_{Iso})$, with $a/b = 1.5$, corresponding to: (a) Left (sloping) face; (b) Front (sloping) face; (c) Right (sloping) face and; Rear (sloping) face.

Figure 16 - Lamination parameter design space surface contours for Positive Shear buckling factor, $k_{xy} (= N_{xy}b^2/\pi^2D_{Iso})$, with $a/b = 2.0$, corresponding to: (a) Left (sloping) face; (b) Front (sloping) face; (c) Right (sloping) face and; Rear (sloping) face.

Tables

Table 1 – Effect of ply continuity constraints ($1, \leq 2, \leq 3$) on number of solutions for each ply number grouping (n), balanced and symmetric representing *Bending-Twisting* coupled designs from databases with the 10% rule applied.

n	<i>Bending-Twisting</i>			10% rule only
	1	≤ 2	≤ 3	
7	4	4	4	4
8	-	6	6	6
9	10	14	18	18
10	-	20	20	24
11	14	30	44	48
12	-	96	104	128
13	68	164	242	260
14	-	392	422	534
15	240	676	980	1,080
16	-	1,572	1,790	2,302
17	690	2,736	4,184	4,612
18	-	6,000	7,142	9,324
19	4,108	10,846	16,842	18,720
20	-	13,532	15,860	19,994
21	5,114	32,116	49,282	53,244

Table 2: Buckling coefficients for Eq. (11), for all discrete mode regions of Fig. 5(c), with $\xi_{11} = 0$ and $a/b = 2.0$.

m	1	2	3	4
c_1	6.2445	3.9946	4.6875	6.2395
c_2	-4.1056	0.0002	1.9754	4.0991
c_3	-0.4533	-1.0428	-0.8605	-0.4529
c_4	-0.0010	-0.0007	-0.0015	-0.0040
c_5	-0.0014	-0.0020	-0.0021	-0.0018
c_6	0.0013	0.0000	-0.0002	-0.0007
c_7	-0.0014	-0.0004	-0.0001	0.0003
c_8	-0.0002	-0.0003	0.0000	0.0000
c_9	-0.0029	-0.0004	0.0000	0.0004
c_{10}	-0.0023	0.0004	0.0003	0.0001
c_{11}	0.0011	0.0000	-0.0002	-0.0006
c_{12}	-0.0003	0.0001	0.0000	-0.0005
c_{13}	0.0013	0.0003	0.0001	-0.0005
c_{14}	0.0008	-0.0002	0.0000	0.0000
c_{15}	0.0015	0.0004	0.0000	-0.0004

Table 3: Coefficients for Eq. (14), representing mode boundaries in Fig. 5(c), with $\xi_{11} = 0$ and $a/b = 2.0$.

	$m_1 = m_2$	$m_2 = m_3$	$m_3 = m_4$
c_1	-3.8053	-3.8280	-10.0172
c_2	6.9129	-11.0256	-32.8008
c_3	0.1197	-0.6705	-45.9682
c_4	-0.1282	-1.2113	-34.0498
c_5	0.0513	-0.8160	-9.4571